JACS
JOURNAL OF THE AMERICAN CHEMICAL SOCIETY
pubs.acs.org/JACS
Article

Non-Bonding Interaction of Neighboring Fe and Ni Single-Atom Pairs on MOF-Derived N-Doped Carbon for Enhanced CO_2 Electroreduction

Long Jiao, Juntong Zhu, Yan Zhang, Weijie Yang, Siyuan Zhou, Aowen Li, Chenfan Xie, Xusheng Zheng, Wu Zhou, Shu-Hong Yu, and Hai-Long Jiang*

Cite This: J. Am. Chem. Soc. 2021, 143, 19417−19424

ABSTRACT: Single-atom catalysts (SACs), featuring high atom utilization, have captured widespread interests in diverse applications. However, the single-atom sites in SACs are generally recognized as independent units and the interplay of adjacent sites is largely overlooked. Herein, by the direct pyrolysis of MOFs assembled with Fe and Ni-doped ZnO nanoparticles, a novel Fe_1−Ni_1−N−C catalyst, with neighboring Fe and Ni single-atom pairs decorated on nitrogen-doped carbon support, has been precisely constructed. Thanks to the synergism of neighboring Fe and Ni single-atom pairs, Fe_1−Ni_1−N−C presents significantly boosted performances for electrocatalytic reduction of CO_2, far surpassing Fe_1−N−C and Ni_1−N−C with separate Fe or Ni single atoms. Additionally, the Fe_1−Ni_1−N−C also exhibits superior performance with excellent CO selectivity and durability in Zn-CO_2 battery. Theoretical simulations reveal that, in Fe_1−Ni_1−N−C, single Fe atoms can be highly activated by adjacent single-atom Ni via non-bonding interaction, significantly facilitating the formation of COOH* intermediate and thereby accelerating the overall CO_2 reduction. This work supplies a general strategy to construct single-atom catalysts containing multiple metal species and reveals the vital importance of the communitive effect between adjacent single atoms toward improved catalysis.

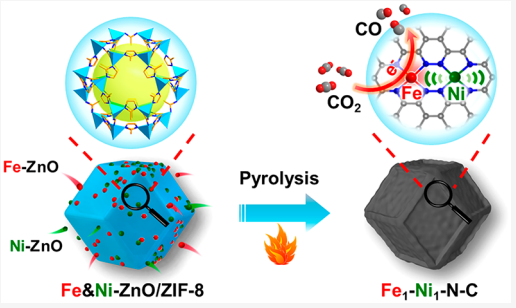

INTRODUCTION

Single-atom catalysts (SACs), a unique heterogeneous catalyst realizing active sites dispersed on the atomic scale, have presented enormous advantages on catalyzing various reactions and have been regarded as promising candidates to mimic the catalytic sites of metalloenzyme to a large extent.[1−7] In the nature enzymes, the adjacent monomers beyond the primary coordination shell, although without direct bonding, can usually interact with each other by their microenvironments and work cooperatively to activate the molecules of interest.[8,9] Taking the Ni−Fe carbon monoxide dehydrogenase (CODH) as an example, the single-atom Fe and Ni sites bridged by sulfide ligands can synergistically catalyze the efficient interconversion of CO_2 and CO under mild conditions.[8] In contrast, the single-atom sites in SACs, even if with enzyme-like structure, are still regarded as isolated units in general; related regulations are mainly based on the change of the atoms directly coordinated with central metal atoms, which is similar to the primary coordination sphere in the enzyme.[10−20] Learning from nature's blueprint, the long-range interaction between adjacent single-atom sites in SACs, which is largely overlooked in current reports, should also be of great significance to catalysis. Despite this, the accurate construction of such adjacent single-atom sites in SACs remains a great challenge and related catalytic investigations are still in their infancy.[21−23]

Metal−organic frameworks (MOFs),[24−27] possessing diverse components and structures, have shown great promises for various applications.[28−32] Particularly, MOFs have been proven to possess superiorities on the precise construction of SACs in recent years.[33−39] Given the great advantages on structural and component regulation, MOFs should be one of the most ideal choices to the construction of SACs with adjacent single-atom sites in a well-controlled manner; unfortunately, very few attempts have been made in this aspect thus far.[21] Among all kinds of MOF-derived SACs, single metal atom decorated nitrogen-doped carbon (M−N−C), with planar and conjugated carbon structures, can readily achieve the long-range electron delocalization[40−42] and is promising to couple adjacent non-bonding single metal atoms. Based on the analysis above, MOF-derived M−N−C,

Received: August 2, 2021
Published: November 15, 2021

https://doi.org/10.1021/jacs.1c08050
J. Am. Chem. Soc. 2021, 143, 19417−19424

integrating both merits of MOFs (ideal platform for the precise construction of SACs) and M−N−C materials (hosts for the interplay between adjacent single-atom sites), would pave a promising way to the accurate construction of adjacent single-atom sites and understanding of their cooperation in catalysis.

Herein, a Zn-assisted atomization strategy (ZAAS) has been developed to incorporate Fe and Ni single atoms to MOF-derived nitrogen-doped carbon (Fe_1−Ni_1−N−C). By the assembly of Fe-doped ZnO (i.e., Fe−ZnO) and Ni-doped ZnO (i.e., Ni-ZnO) nanoparticles (NPs) onto ZIF-8 (ZIF = zeolitic imidazolate framework) via electrostatic interaction, the Fe&Ni-ZnO/ZIF-8 composite can be facilely obtained. Upon pyrolysis, ZnO can be reduced to Zn and evaporated away, affording ZIF-8 derived nitrogen-doped carbon implanted by adjacent Fe−N_4 and Ni−N_4 sites (denoted Fe_1−Ni_1−N−C; Scheme 1). Thanks to the long-range

Scheme 1. Schematic Illustration for Construction of Fe_1−Ni_1−N−C with Neighboring Fe and Ni Single-Atoms Based on ZIF-8

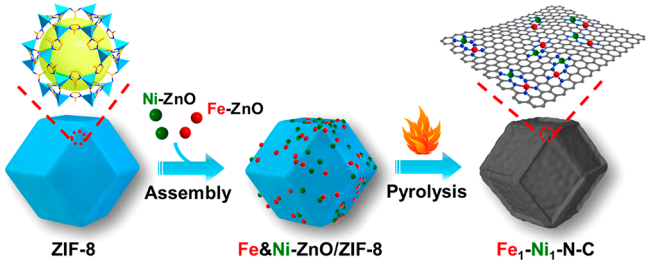

electronic interaction of adjacent Fe and Ni single-atom pairs, Fe_1−Ni_1−N−C presents enhanced performance for CO_2 electroreduction achieving Faradaic efficiency (FE) of 96.2% at −0.5 V, superior to those of nitrogen-doped carbon supports decorated with Fe or Ni single atoms only, denoted as Fe_1−N−C and Ni_1−N−C. Theoretical simulations suggest, by coupling neighboring Ni and Fe single atoms in Fe_1−Ni_1−N−C, it can benefit CO_2 activation and reduce formation energy barrier for COOH* intermediate, surpassing Fe_1−N−C or Ni_1−N−C, which greatly improves CO_2 reduction performance of Fe_1−Ni_1−N−C.

RESULTS AND DISCUSSION

Synthesis and Characterizations of Fe_1−Ni_1−N−C. The ZIF-8 precursor, also called MAF-4, was synthesized by the assembly of Zn^{2+} and 2-methylimidazole (Figure S1).[43,44] Scanning electron microscope (SEM) and TEM images illustrate rhombic dodecahedral morphology of ZIF-8 with an average size of 250 nm (Figure S2). Then, Fe-ZnO and Ni-ZnO NPs with positive surface charges were synthesized and co-assembled onto negatively charged ZIF-8 via electrostatic interaction (Figures S3 and S4). It can be seen clearly that the Fe-ZnO and Ni-ZnO NPs, illustrating the particle sizes of ∼5 nm, were successfully attached outside of ZIF-8, leading to a Fe&Ni-ZnO/ZIF-8 composite with retained morphology and crystallinity of ZIF-8 (Figures S1, S5, and S6). Via direct pyrolyzation of Fe&Ni-ZnO/ZIF-8, ZIF-8 can be transformed to nitrogen-doped porous carbon. Meanwhile, ZnO NPs can be reduced to metallic Zn (boiling point: 907 °C) by the carbon and evaporated away easily along the carrier gas flow.[45] The CO and CO_2 gases detected during the pyrolysis process further confirms the carbon thermal reduction of ZnO (Figure S7). Finally, the doped Fe and Ni atoms in ZnO were captured by N-doped carbon, yielding Fe_1−Ni_1−N−C material with retained polyhedral morphology (Figure 1a,b). The elemental

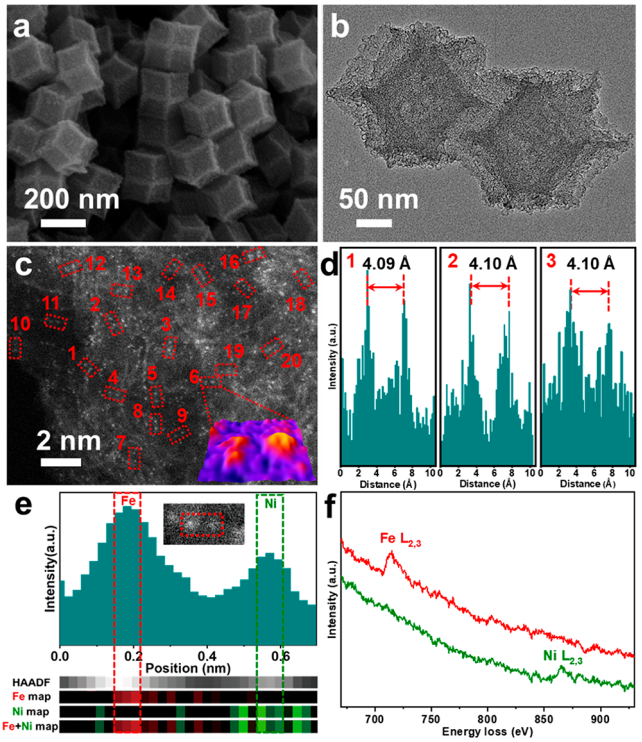

Figure 1. Microscopic characterizations. (a) SEM and (b) transmission electron microscope (TEM) images of Fe_1−Ni_1−N−C. (c) Aberration-corrected HAADF-STEM observation for Fe_1−Ni_1−N−C (inset: 3D atom-overlapping Gaussian-function fitting map of region 6 in panel c). (d) Line-scanning intensity profiles obtained from the region 1−3 highlighted in panel c. (e) Simultaneously acquired HAADF-STEM image intensity profile accompanied by atomic-resolution EELS mapping of the Fe−Ni pair presented in panel e. (f) Single-atom EELS spectra extracted from two atomic positions highlighted in red and green in panel e.

mapping demonstrates the homogeneous dispersion of Fe and Ni elements on the carbon support in Fe_1−Ni_1−N−C (Figure S8). There is no apparent Fe or Ni NPs in Fe_1−Ni_1−N−C as is observed in the TEM image (Figure 1b). Only two broad peaks centered on ∼26° and 44° for Fe_1−Ni_1−N−C, which are (002) and (101) crystal faces of carbon, are found in powder X-ray diffraction (XRD) analysis, further excluding crystalline metal species formation (Figure S9). N_2 sorption isotherm suggests that Fe_1−Ni_1−N−C possesses large surface area (595 m^2/g) with highly porous feature (Figure S10), which could benefit catalytic sites exposure and accelerate substrates/products transfer within catalysts.

The aberration-corrected high-angle annular dark-field scanning transmission electron microscopy (HAADF-STEM) detection for Fe_1−Ni_1−N−C illustrates isolated dispersion of Fe and Ni atoms and a large part of the bright spots come in pairs (typically circled by red boxes), consequently named as single-atom pairs (SAPs; Figures 1c and S11). Three-dimensional (3D) atom-overlapping Gaussian-function fitting mappings in Figures 1c and S12a clearly present the existence of atom pairs (Figures 1c and S12). In addition, the distances of atom pairs identified by the intensity profiles in the 20 randomly selected regions of Figure 1c are all close to ∼4.1 Å,

https://doi.org/10.1021/jacs.1c08050
J. Am. Chem. Soc. 2021, 143, 19417−19424

verifying the formation of particular SAPs in Fe_1-Ni_1-N-C (Figures 1d and S13). Furthermore, the atomic-resolution elemental analysis via electron energy-loss spectroscopy (EELS) line-scan clearly shows the single-atom pair analyzed contains one Fe atom and one Ni atom, strongly confirming the Fe−Ni single-atom pairs formation in Fe_1-Ni_1-N-C (Figure 1e,f). The Fe and Ni loadings in Fe_1-Ni_1-N-C are 0.45 and 0.42 wt %, suggesting an Fe/Ni molar ratio of ∼1:1 (Table S1). For better comparison, Fe_1-N-C (with only single Fe atoms) and Ni_1-N-C (with only single Ni atoms), with similar Fe or Ni loadings, N contents, morphology, graphitization degree, and porous structure to Fe_1-Ni_1-N-C, have been also constructed in a similar way, respectively from Fe-ZnO/ZIF-8 and Ni-ZnO/ZIF-8 (Figures S14 and S15 and Table S1). As is shown in Figure S16, Fe_1-N-C and Ni_1-N-C possessing single metal species, present only isolated atoms on carbon support and no atom pairs can be observed (Figure S16). This is in stark contrast with the formation of SAPs when Fe and Ni are coexisted, implying that heteroatom Fe−Ni pairs are formed in Fe_1-Ni_1-N-C.

X-ray photoelectron spectroscopy (XPS) is implemented for identification of chemical compositions in Fe_1-Ni_1-N-C and their corresponding electronic states. The N 1s spectrum of Fe_1-Ni_1-N-C is fitted by four peaks and metal-N peak manifests the existence of metal−nitrogen coordination configurations (Figure S17).[46] The near-edge X-ray absorption fine structure (NEXAFS) spectrum of N K-edge for Fe_1-Ni_1-N-C suggests an evident absorption at ∼400.1 eV, further proving the formation of metal−nitrogen bonding (Figure S18).[37] The Fe $2p_{3/2}$ peaks of Fe_1-Ni_1-N-C and Fe_1-N-C locate between Fe^{2+} (709.6 eV) and Fe^{3+}(711.6 eV), manifesting the partially oxidative state of Fe (Figure 2a).[12]

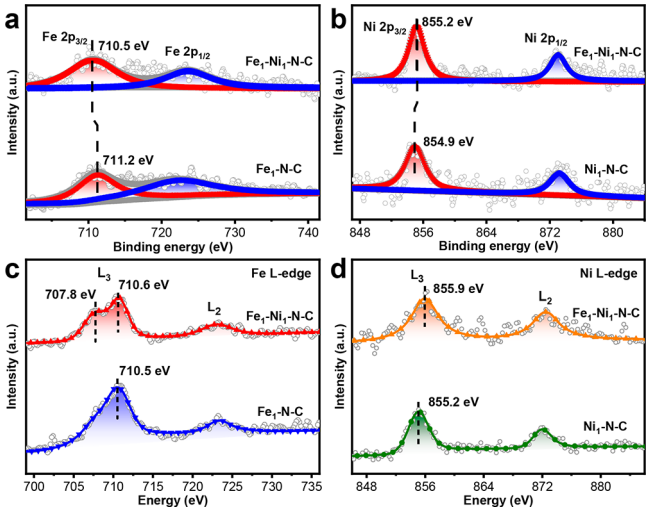

Figure 2. Valence state analysis. (a) Fe 2p spectra and (c) Fe L-edge NEXAFS spectra for Fe_1-Ni_1-N-C and Fe_1-N-C. (b) Ni 2p spectra and (d) Ni L-edge NEXAFS spectra for Fe_1-Ni_1-N-C and Ni_1-N-C.

Similarly, in Figure 2b, the valence states of Ni on Fe_1-Ni_1-N-C and Ni_1-N-C also locate between 0 (853.0 eV) and +2 (855.7 eV), exhibiting its partially oxidized state.[37] The binding energy of Fe $2p_{3/2}$ in Fe_1-Ni_1-N-C is revealed to shift by −0.7 eV compared with that in Fe_1-N-C (Figure 2a). Meanwhile, Ni $2p_{3/2}$ in Fe_1-Ni_1-N-C shifts to a higher energy by +0.3 eV than that in Ni_1-N-C. The XPS results suggest that, in Fe_1-Ni_1-N-C, the Ni atoms donate partial electrons to Fe (Figure 2b). To further clarify the electronic states of Fe and Ni in Fe_1-Ni_1-N-C, the NEXAFS analysis for Fe and Ni has been performed. The Fe L-edge of Fe_1-N-C shows a dominate peak at 710.5 eV at the L_3 region assignable to Fe^{3+} (Figure 2c).[47] In contrast to Fe L-edge of Fe_1-N-C, the shoulder peak at relatively smaller energy (707.8 eV) becomes more prominent in Fe_1-Ni_1-N-C, implying that Fe is partially reduced in Fe_1-Ni_1-N-C (Figure 2c).[47] On the contrary, Fe_1-Ni_1-N-C illustrates a positively shifted Ni L-edge compared with Ni_1-N-C, manifesting a higher valence of Ni in Fe_1-Ni_1-N-C (Figure 2d). Therefore, the L-edge NEXAFS spectra, accompanied by the XPS results, present solid evidences for the existence of long-range electronic interaction between adjacent Fe and Ni atom in Fe_1-Ni_1-N-C, and the interaction between Fe and Ni might serve as the intrinsic driven force to form Fe−Ni pairs.

Atomic Structure Analysis. To further identify chemical environments of Fe and Ni atoms, the X-ray absorption fine structure (XAFS) spectroscopy was performed. The X-ray absorption near-edge structure (XANES) spectrum for Fe K-edge of Fe_1-Ni_1-N-C sits in the middle of Fe_2O_3 and Fe, proving the valence of Fe is positive lower than +3 (Figure 3a). Similarly, XANES spectrum of Ni K-edge for Fe_1-Ni_1-N-C confirms that the Ni oxidation state locates between 0 and +2 (Figure S19a), in good accordance with XPS analysis above. Moreover, in XANES spectra of Fe K-edge, Fe_1-Ni_1-N-C

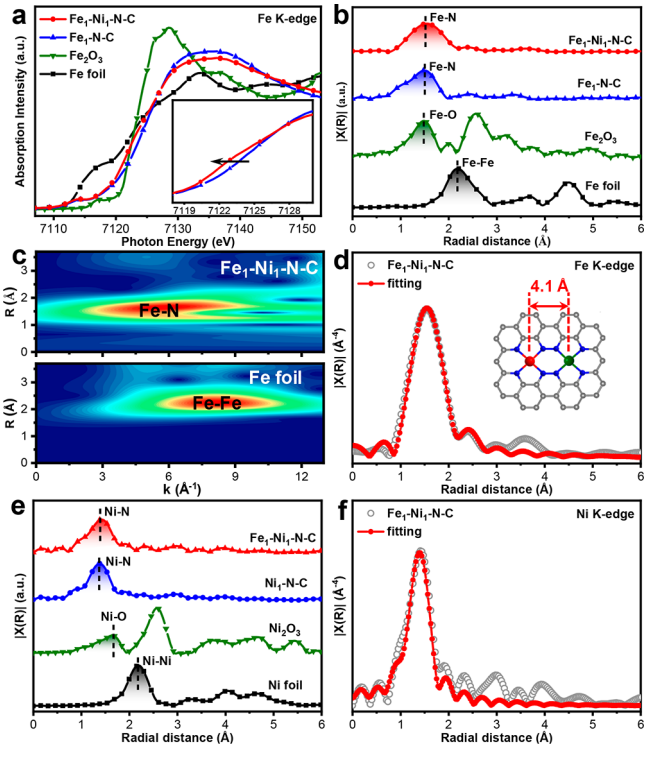

Figure 3. Structure characterizations. (a) Fe K-edge XANES, (b) Fourier transform-extended X-ray absorption fine structure (FT-EXAFS) spectra of Fe_1-Ni_1-N-C and Fe_1-N-C. (c) WT plots for Fe element of Fe_1-Ni_1-N-C and Fe foil. (d) Fe K-edge EXAFS spectrum fitting of Fe_1-Ni_1-N-C and (inset) optimized configuration for Fe (the blue, gray, red, and green spheres represent N, C, Fe, and Ni atoms). (e) Ni K-edge FT-EXAFS spectra of Fe_1-Ni_1-N-C and Ni_1-N-C. (f) Ni K-edge EXAFS spectrum fitting of Fe_1-Ni_1-N-C.

https://doi.org/10.1021/jacs.1c08050
J. Am. Chem. Soc. 2021, 143, 19417−19424

shows a bit lower adsorption edge than Fe_1−N−C, suggesting the decreased valence of Fe in Fe_1−Ni_1−N−C (Figure 3a). In contrast, in Ni K-edge XANES spectra, the Fe_1−Ni_1−N−C exhibits a positive energy shift relative to Ni_1−N−C (Figure S19a). The energy shifts of Fe and Ni in XANES spectra agree well with the electron transfer from Ni to Fe, in line with the above observation of XPS and L-edge NEXAFS analysis.

Furthermore, both FT-EXAFS analysis for Fe in Fe_1−Ni_1−N−C and Fe_1−N−C show similar peaks around 1.49 Å originating from Fe−N bonding (Figure 3b). Fe−Fe or Fe−Ni bonding is absent confirming that Fe atoms disperse atomically on Fe_1−Ni_1−N−C and Fe_1−N−C (Figure 3b). Moreover, EXAFS wavelet transform (WT) analysis for Fe_1−Ni_1−N−C and Fe_1−N−C presents similar single intensity maximum assignable to Fe−N path at around 4.7 $Å^{-1}$ (Figures 3c and S20). The EXAFS fittings further confirm the $Fe-N_4$ configuration of Fe in both Fe_1−Ni_1−N−C and Fe_1−N−C (Figures 3d and S21, Table S2). Moreover, Ni K-edge EXAFS spectra analysis as well as curve fittings for Fe_1−Ni_1−N−C and Ni_1−N−C also demonstrates that Ni atoms are atomically dispersed with $Ni-N_4$ configuration (Figures 3e,f, S19b, and S22 and Table S3).

Considering electron microscopy and XAFS results above, different structural models have been constructed by theoretical simulations (Figure S23). Among all simulated structures, the Fe−N−N−Ni model, with the most consistent coordination environment and interatomic distance (~4.1 Å) to experimental fitting results, has been demonstrated as the most optimized structure of the active unit in Fe_1−Ni_1−N−C (Figures 3d and S23). For better comparison, the nitrogen-doped carbon (N−C) without Fe/Ni species was also obtained by pyrolyzing the composite of pure ZnO supported on ZIF-8 (ZnO/ZIF-8; Figures S1 and S9).

Electrocatalytic Performance for CO_2RR. Based on the analysis above, the electrocatalytic CO_2 reduction reaction (CO_2RR) measurements of the prepared catalysts have been performed. The linear scanning voltammetry (LSV) measurements reveal that all samples show higher current responses under CO_2 atmosphere compared with those under nitrogen, manifesting their catalytic activities for CO_2RR (Figures S24−S27). Notably, Fe_1−Ni_1−N−C with adjacent Fe and Ni SAPs shows much higher current density for CO_2RR than Fe_1−N−C, Ni_1−N−C, as well as metal-free N−C (Figure 4a). Moreover, Fe_1−Ni_1−N−C gives an ultrahigh CO selectivity (96.2%@-0.5 V) while Fe_1−N−C and N−C present inferior CO FE to Fe_1−Ni_1−N−C in all potential ranges (Figure 4b). Ni_1−N−C, although with the maximum CO selectivity comparable to Fe_1−Ni_1−N−C, requires a more negative potential (−0.65 V), which is more energy-consuming than Fe_1−Ni_1−N−C (Figure 4b). For all tested samples, CO and H_2 are the main products with the total FE close to 100% in the applied potentials and no liquid product is detected (Figures 4b, S28, and S29). Meanwhile, Fe_1−Ni_1−N−C achieves superior CO partial current density (J_{CO}; 2.4 mA/cm^2@-0.5 V) to Fe_1−N−C (2.1 mA/cm^2), Ni_1−N−C (0.1 mA/cm^2), and N−C (0.7 mA/cm^2; Figure 4c). Fe_1−Ni_1−N−C displays smaller tafel slope (83 mV/dec) than Fe_1−N−C, Ni_1−N−C, and N−C, illustrating a faster kinetics of Fe_1−Ni_1−N−C for CO_2RR (Figure S30). The superior CO_2RR activities of Fe_1−Ni_1−N−C compared to Fe_1−N−C and Ni_1−N−C with Fe or Ni single atoms only, manifesting great superiority of Fe_1−Ni_1−N−C with neighboring Fe and Ni atoms. Moreover, Fe_1−Ni_1−N−C shows similar electrochemical

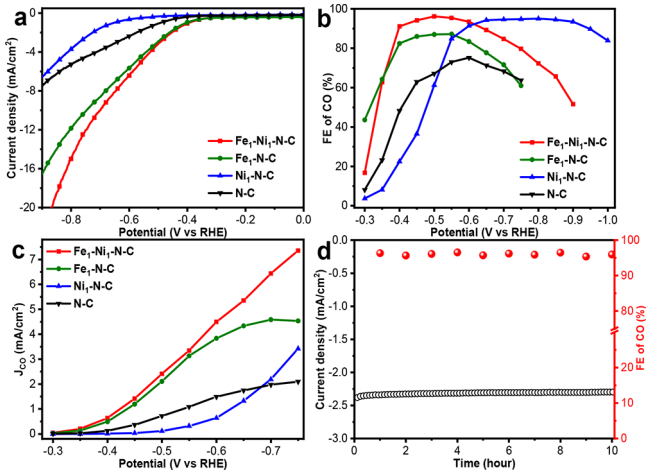

Figure 4. Electrochemical performances for CO_2 reduction. (a) LSV tests, (b) FEs of CO, (c) the J_{CO} for Fe_1−Ni_1−N−C, Fe_1−N−C, Ni_1−N−C, and N−C in 0.5 M $KHCO_3$. (d) The stability measurement for Fe_1−Ni_1−N−C at −0.5 V.

active surface area (ECSA) as well as BET surface area to Ni_1−N−C and Fe_1−N−C, further supporting that the better CO_2RR performance originates from better intrinsic activity of Fe−Ni pairs in Fe_1−Ni_1−N−C rather than the variation of surface area (Figures S10 and S31). In addition, the physical mixture of Fe_1−N−C and Ni_1−N−C (mix-Fe_1−N−C/Ni_1−N−C), without interplay between Fe and Ni atoms, also shows much inferior CO_2RR activity to Fe_1−Ni_1−N−C (Figure S32). Besides, when the single Ni atoms are replaced by Co atoms, the obtained Fe_1−Co_1−N−C catalyst shows inferior CO selectivity due to the significant hydrogen evolution activity of Co sites (Figure S33). The results above clearly demonstrate that the significant synergy between Fe and Ni atoms contributes to superior CO_2RR performance of Fe_1−Ni_1−N−C. When nitrogen-doped carbon obtained from ZIF-8 is replaced by commercial acetylene black (AB) to loading Fe and Ni atoms, obvious Ni and Fe agglomerations can be observed on the Fe−Ni/AB composite due to the absence of N anchoring sites (Figure S34a). As a result, Fe−Ni/AB presents inferior CO selectivity in the CO_2 reduction, further illustrating the superiority of nitrogen-doped carbon obtained from ZIF-8 for the stabilization of single atoms (Figure S34b). Moreover, Fe_1−Ni_1−N−C can be continuously operated at −0.5 V for 10 h with nearly unchanged current density and FE of CO, exhibiting its excellent stability for CO_2RR (Figure 4d).

Due to the superior CO_2RR performance, Fe_1−Ni_1−N−C was further performed in rechargeable Zn−CO_2 battery. The Fe_1−Ni_1−N−C, as a cathode catalyst, is put in $KHCO_3$ solution to proceed CO_2RR when supplied with CO_2 and the Zn anode is immersed in 6 M KOH (Figure 5a).[46,48] The charge and discharge voltages under different current densities clearly manifest the rechargeable behavior of assembled Zn-CO_2 battery (Figure S35). Meanwhile, the CO_2RR products during discharge process are also detected. It is shown that Fe_1−Ni_1−N−C equipped in the Zn-CO_2 battery presents excellent selectivity to CO with a maximized FE up to 93.4% at 1 mA and the excellent FE of CO can be largely maintained in a wide range of current (Figure 5b). Furthermore, Fe_1−Ni_1−N−C shows good stability over 15 h under continuous discharge−charge processes, manifesting the excellent stability of the assembled Zn-CO_2 battery (Figure 5c).

https://doi.org/10.1021/jacs.1c08050
J. Am. Chem. Soc. 2021, 143, 19417−19424

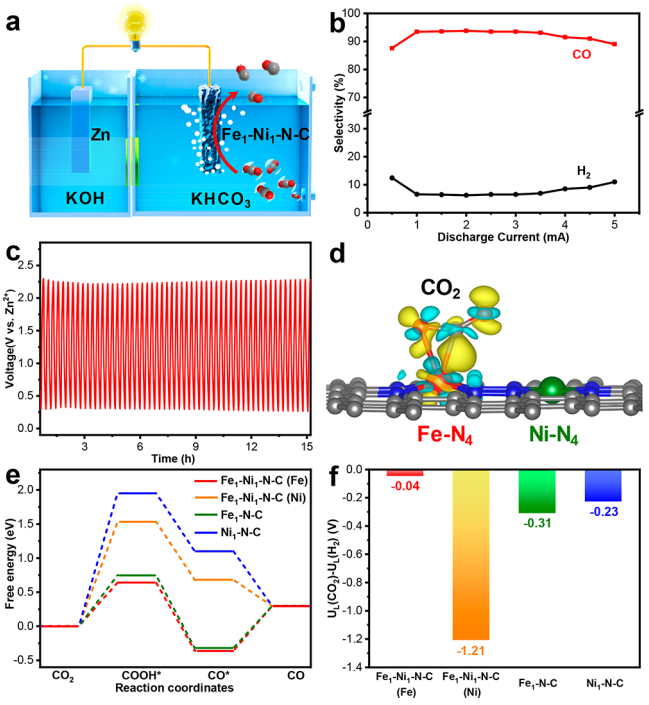

Figure 5. Zn-CO_2 battery measurements and DFT calculations. (a) Illustration for the aqueous rechargeable Zn-CO_2 battery employing Fe_1−Ni_1−N−C at the cathode. (b) FE of CO and H_2 under various discharge currents. (c) Discharge−charge stability test at 1.1 mA. (d) Electron density difference analysis of CO_2 adsorbed on Fe−N_4 sites of Fe_1−Ni_1−N−C (yellow and cyan stands for charge accumulation and depletion). (e) Free energy diagrams of CO_2RR and (f) The $U_L(CO_2) - U_L(H_2)$ values of Fe and Ni sites in different samples.

Theoretical Study of Fe_1−Ni_1−N−C for CO_2RR. DFT calculations have been conducted to reveal the cooperative mechanism of adjacent Fe−N_4 and Ni−N_4 sites on enhancing CO_2RR performance of Fe_1−Ni_1−N−C. When CO_2 is adsorbed on Fe sites in Fe_1−Ni_1−N−C, the linear configuration is distorted with a bending angle of 147°, and electron density difference analysis demonstrates the enriched electron density in the region between Fe and CO_2, indicating the superiority of Fe sites of Fe_1−Ni_1−N−C for CO_2 activation (Figure 5d).

Generally, the CO_2 reduction to CO is a process calling for two electrons and COOH* is generally regarded as potential-determining intermediate.[49−51] The free-energy change of COOH* formation on Fe sites in Fe_1−Ni_1−N−C (Fe_1−Ni_1−N−C(Fe)) is 0.64 eV, much lower than their adjacent Ni sites (Fe_1−Ni_1−N−C(Ni); 1.53 eV) as well as Ni_1−N−C (1.95 eV) and Fe_1−N−C (0.75 eV; Figure 5e). The results above unambiguously prove that the CO_2RR performance of Fe sites is greatly enhanced via their adjacent Ni−N_4 sites. Moreover, the free-energy changes for hydrogen production, as the competing reaction for CO_2RR, are further investigated. Fe_1−Ni_1−N−C(Fe) presents much higher energy barrier than Fe_1−N−C for hydrogen production (Figure S36). Then, $U_L(CO_2) - U_L(H_2)$, representing limiting potential difference of CO_2RR and H_2 evolution, is further used as an indicator and more positive $U_L(CO_2) - U_L(H_2)$ indicates better selectivity toward CO.[37,49] As shown in Figure 5f, the Fe site in Fe_1−Ni_1−N−C presents the most positive value (−0.04 eV) among all calculated sites, further supporting the higher CO selectivity of Fe_1−Ni_1−N−C.

CONCLUSIONS

To sum up, a novel and facile Zn-assisted atomization method is put forward to construct a single-atom Fe_1−Ni_1−N−C catalyst with N-bridged Fe and Ni SAPs. The obtained Fe_1−Ni_1−N−C catalyst achieves ultrahigh CO FE (96.2%) under the potential of −0.5 V, far surpassing Fe_1−N−C and Ni_1−N−C with isolated Fe or Ni sites. Moreover, the Fe_1−Ni_1−N−C has been further used as a cathode catalyst for the Zn-CO_2 battery, exhibiting excellent FE of CO and operation durability. Mechanism investigations reveal that the N-bridged single-atom Fe and Ni sites in Fe_1−Ni_1−N−C can work synergistically to facilitate CO_2 adsorption and lower the formation energy barrier of COOH* leading to the enhanced CO_2RR performance. This work develops a universal strategy to construct SAPs. Meanwhile, it creates new opportunities to optimize performances of single-atom catalysts via manipulating interplay of adjacent single-atom sites.

EXPERIMENTAL SECTION

Synthesis of ZIF-8. The synthesis method follows the previous report with some modifications.[46,52] First, the $Zn(NO_3)_2{\cdot}6H_2O$ (1.116 g) in methanol (30 mL) was mixed with methanol (30 mL) solution of 2-methylimidazole (1.232 g). After being sonicated for 6 min, the mixture was put into a 100 mL Teflon reactor, which is then reacted under 120 °C for 2 h. After natural cooling, the white powders were obtained via centrifugation and washed by methanol three times. Then the as-obtained precipitates were put in a vacuum oven at 60 °C overnight.

Synthesis of M-ZnO (M = Fe, Co, Ni) and ZnO NPs. The synthesis follows a previous report with some modifications.[53] Taking the synthesis of Fe-ZnO/ZIF-8 as an example, $Zn(CH_3COO)_2{\cdot}2H_2O$ (550 mg) and $Fe(CH_3COO)_2$ (22 mg) were dissolved in 25 mL of dimethylsulfoxide (DMSO) first. Then 7.7 mL of ethanol solution of tetramethylammonium hydroxide pentahydrate (0.1 g/mL) was gradually droped into the above DMSO solution within 1.5 min under stirring. After the addition of 60 mL of ethyl acetate, the Fe-ZnO NPs were isolated by centrifugation and redispersed into 6 mL of ethanol, affording the ethanol solution of Fe-ZnO NPs (25 mg/mL). The ethanol solution of Ni-ZnO NPs (20 mg/mL) or Co-ZnO NPs (20 mg/mL) was obtained following the same procedure as Fe-ZnO NPs except for $Ni(CH_3COO)_2{\cdot}4H_2O$ (31 mg) or $Co(CH_3COO)_2{\cdot}4H_2O$ (31 mg) was used instead of $Fe(CH_3COO)_2$. The ZnO NPs (25 mg/mL) were synthesized following the same procedure as Fe-ZnO NPs without the addtion of $Fe(CH_3COO)_2$.

Synthesis of Fe&Ni-ZnO/ZIF-8, M-ZnO/ZIF-8 (M = Fe, Co, Ni), ZnO/ZIF-8, and Fe&Co-ZnO/ZIF-8. For Fe&Ni-ZnO/ZIF-8 synthesis, ZIF-8 (90 mg) was introduced into 9 mL of ethanol and ultrasonically dispersed for 5 min. Then, the mixture of Fe-ZnO solution (800 μL) and Ni-ZnO solution (400 μL) was injected to the dispersion solution of ZIF-8, respectively. After being stirred for 10 h, faint yellow powders were collected by centrifuging and dried at 60 °C. The Fe-ZnO/ZIF-8 and Ni-ZnO/ZIF-8 can also be prepared through similar procedures to Fe&Ni-ZnO/ZIF-8 by using a mixture containing Fe-ZnO (800 μL) and ZnO solutions (400 μL) or the mixture of a ZnO solution (800 μL) and a Ni-ZnO solution (400 μL), respectively. The ZnO/ZIF-8 was obtained through a similar procedure by adding a pure ZnO solution (1200 μL) only. The Fe&Co-ZnO/ZIF-8 and Co-ZnO/ZIF-8 have been obtained via similar procedures to Fe&Ni-ZnO/ZIF-8 by using a mixture containing the Fe-ZnO (800 μL) and Co-ZnO solutions (400 μL) or the mixture of the ZnO (800 μL) and Co-ZnO solutions (400 μL), respectively.

Synthesis of Fe_1−Ni_1−N−C, M_1−N−C (M = Fe, Co, Ni), and N−C. For Fe_1−Ni_1−N−C preparation, Fe&Ni-ZnO/ZIF-8 powders (500 mg) were pyrolyzed under 900 °C for 2 h in nitrogen. After natural cooling, Fe_1−Ni_1−N−C powders were finally obtained. The M_1−N−C and N−C could be obtained similar to Fe_1−Ni_1−N−C by

https://doi.org/10.1021/jacs.1c08050
J. Am. Chem. Soc. 2021, 143, 19417−19424

the pyrolysis of M-ZnO/ZIF-8 (M = Fe, Co, Ni) and ZnO/ZIF-8 composites, respectively.

Synthesis of Fe−Ni/AB. Commercial acetylene black (90 mg) was introduced into 9 mL of ethanol and ultrasonically dispersed for 5 min. Then, the mixture of the Fe-ZnO (800 μL) and Ni-ZnO solutions (400 μL) were injected to the dispersion solution of acetylene black. After being stirred for 10 h, powders were separated and dried at 60 °C, which were then pyrolyzed in nitrogen under 900 °C for 2 h and Fe−Ni/AB powders were finally obtained.

Characterizations. Powder XRD measurements were performed on Japan Rigaku Miniflex 600 using Cu Kα radiation. N_2 sorption analysis were carried out at 77 K using the Micromeritics ASAP 2020 system. TEM were carried out on JEM-2010. Aberration-corrected HAADF-STEM observations were implemented using JEM-ARM200F at 200 keV. SEM observations were realized on Zeiss Supra 40. A Renishaw System 2000 spectrometer was used to obtain Raman scattering spectra excited by 514.5 nm line. Zeta potential measurements were made using the zeta potential analyzer (Zetasizer Nano ZSE, Malvern, U.K.) using ethanol as the solvent. The metal contents were quantified on an Optima 7300 DV instrument. XPS analysis was performed by an ESCALAB 250 electron spectrometer with the excitation source of monochromatized Al Kα. Thermogravimetry-mass spectrometry (TG-MS) was performed using a PerkinElmer TGA and mass spectrometer. Atomic-resolution EELS analysis was implemented by Nion HERMES-100 STEM with a C3/C5 corrector, working under 60 kV with convergence and collection semiangles of ∼32 and ∼75 mrad. The HAADF *Z*-contrast image was collected in the identical region employing an annular detector with a range of 75−210 mrad. To illustrate Fe $L_{2,3}$ edge and Ni $L_{2,3}$ edge signal dispersions, the EELS mapping with a probe current of ∼15 pA was performed, sampling with a dwell time of 150 ms per pixel and a pixel size of ∼0.02 nm. Principal component analysis was used for the raw data of experiments using MSA plugin for Gatan's Digital Micrograph to optimize signal-to-noise ratio of datum obtained by EELS.[54]

Electrochemical Analysis. CHI 760E electrochemical workstations were employed to implement electrocatalytic analysis. H-type cell divided by a cation exchange membrane (Nafion115, dupont) was used to perform CO_2 electrochemical reduction. The scan rate for LSV measurements is 5 mV/s. All potentials were calculated to vs RHE from vs Ag/AgCl via adding 0.197 + 0.059 × pH. The electrochemical data are all illustrated without *i*R compensation.

The catalyst powders (5 mg) were mixed with 20 μL of Nafion (5 wt %) and 1 mL of ethanol. After being sonicated for 10 min, 60 μL of ink was sprayed on carbon paper (1.0 × 1.0 cm^2). The gas products were detected by GC per 30 min. Quantifications for produced gas were realized by thermal conductivity and flame ionization detectors. Nuclear magnetic resonance (NMR) measurements were used for detection of liquid product, and a solvent presaturation method was employed to suppress the water peak.

Zn-CO_2 Battery. The rechargable Zn-CO_2 battery tests were carried out using H-cell divided by bipolar membrane. The KOH (0.8 M) and $Zn(CH_3COO)_2$ (0.02 M) were filled in the anode compartment, and the cathodic electrolyte was 0.8 M $KHCO_3$. The cathode compartment was bubbled with CO_2 at 20 mL/min during the measurements. A Zn plate (2 × 5 cm^2) was polished and employed as the anode electrode. The measurement for the cell was implemented by a cell testing instrument (CT2001A, LANHE).

X-ray Adsorption Spectra. The NEXAFS spectroscopy measurements for N, Fe, and Ni were performed in total electron yield (TEY) mode at the BL10B station of NSRL.

The XANES and EXAFS analysis for the Fe/Ni K-edge was performed at the 1W1B station of BSRF and 14WB1 beamline of SSRF. All data of metal foils were obtained via transmission mode and other catalysts were tested using fluorescence mode. Data analysis was implemented on Athena and Artemiss software packages. Energy calibration was performed based on metal foils. For EXAFS modeling, EXAFS of the metal foil was fitted, and the obtained amplitude reduction factor S_0^2 value was set for the EXAFS fitting to determine coordination numbers (CNs) of the M-N scattering path in different samples.

■ ASSOCIATED CONTENT

Supporting Information

The Supporting Information is available free of charge at https://pubs.acs.org/doi/10.1021/jacs.1c08050.

Additional experimental materials and details, XRD results, SEM and TEM images, Raman spectra, XPS analysis, zeta potential, TG-MS measurement, XAFS spectra, N_2 sorption isotherm, electrochemical measurements, and DFT calculations (PDF)

■ AUTHOR INFORMATION

Corresponding Author

Hai-Long Jiang − *Hefei National Laboratory for Physical Sciences at the Microscale, CAS Key Laboratory of Soft Matter Chemistry, Department of Chemistry, University of Science and Technology of China, Hefei, Anhui 230026, P. R. China;* orcid.org/0000-0002-2975-7977; Email: jianglab@ustc.edu.cn

Authors

Long Jiao − *Hefei National Laboratory for Physical Sciences at the Microscale, CAS Key Laboratory of Soft Matter Chemistry, Department of Chemistry, University of Science and Technology of China, Hefei, Anhui 230026, P. R. China*

Juntong Zhu − *School of Physical Sciences and CAS Key Laboratory of Vacuum Physics, University of Chinese Academy of Sciences, Beijing 100049, P. R. China*

Yan Zhang − *Hefei National Laboratory for Physical Sciences at the Microscale, CAS Key Laboratory of Soft Matter Chemistry, Department of Chemistry, University of Science and Technology of China, Hefei, Anhui 230026, P. R. China*

Weijie Yang − *Department of Power Engineering, School of Energy, Power and Mechanical Engineering, North China Electric Power University, Baoding, Hebei 071003, P. R. China*

Siyuan Zhou − *School of Physical Sciences and CAS Key Laboratory of Vacuum Physics, University of Chinese Academy of Sciences, Beijing 100049, P. R. China*

Aowen Li − *School of Physical Sciences and CAS Key Laboratory of Vacuum Physics, University of Chinese Academy of Sciences, Beijing 100049, P. R. China*

Chenfan Xie − *Hefei National Laboratory for Physical Sciences at the Microscale, CAS Key Laboratory of Soft Matter Chemistry, Department of Chemistry, University of Science and Technology of China, Hefei, Anhui 230026, P. R. China*

Xusheng Zheng − *National Synchrotron Radiation Laboratory, University of Science and Technology of China, Hefei, Anhui 230029, P. R. China*

Wu Zhou − *School of Physical Sciences and CAS Key Laboratory of Vacuum Physics, University of Chinese Academy of Sciences, Beijing 100049, P. R. China; CAS Center for Excellence in Topological Quantum Computation, University of Chinese Academy of Sciences, Beijing 100049, P. R. China*

Shu-Hong Yu − *Hefei National Laboratory for Physical Sciences at the Microscale, CAS Key Laboratory of Soft Matter Chemistry, Department of Chemistry, University of Science and Technology of China, Hefei, Anhui 230026, P. R. China;* orcid.org/0000-0003-3732-1011

Complete contact information is available at:
https://pubs.acs.org/10.1021/jacs.1c08050

Notes

The authors declare no competing financial interest.

■ ACKNOWLEDGMENTS

This work is supported by the NSFC (21725101, 22161142001, 21521001, and 22001242), Beijing Outstanding Young Scientist Program (BJJWZYJH01201914430039), International Partnership Program of CAS (211134KYSB20190109), and Collaborative Innovation Program of Hefei Science Center, CAS (2020HSC-CIP005). We thank 1W1B station at BSRF and BL14W1 station at SSRF for XAFS measurements and BL10B at NSRL for NEXAFS measurements.

■ REFERENCES

(1) Wang, A.; Li, J.; Zhang, T. Heterogeneous Single-Atom Catalysis. *Nat. Rev. Chem.* **2018**, *2*, 65−81.
(2) Huang, L.; Chen, J.; Gan, L.; Wang, J.; Dong, S. Single-Atom Nanozymes. *Sci. Adv.* **2019**, *5*, No. eaav5490.
(3) Jiao, L.; Yan, H.; Wu, Y.; Gu, W.; Zhu, C.; Du, D.; Lin, Y. When Nanozymes Meet Single-Atom Catalysis. *Angew. Chem., Int. Ed.* **2020**, *59*, 2565−2576.
(4) Liu, L.; Corma, A. Metal Catalysts for Heterogeneous Catalysis: From Single Atoms to Nanoclusters and Nanoparticles. *Chem. Rev.* **2018**, *118*, 4981−5079.
(5) Hannagan, R. T.; Giannakakis, G.; Flytzani-Stephanopoulos, M.; Sykes, E. C. H. Single-Atom Alloy Catalysis. *Chem. Rev.* **2020**, *120*, 12044−12088.
(6) Peng, Y.; Lu, B.; Chen, S. Carbon-Supported Single Atom Catalysts for Electrochemical Energy Conversion and Storage. *Adv. Mater.* **2018**, *30*, 1801995.
(7) Ji, S.; Chen, Y.; Wang, X.; Zhang, Z.; Wang, D.; Li, Y. Chemical Synthesis of Single Atomic Site Catalysts. *Chem. Rev.* **2020**, *120*, 11900−11955.
(8) Jeoung, J.-H.; Dobbek, H. Carbon Dioxide Activation at the Ni, Fe-Cluster of Anaerobic Carbon Monoxide Dehydrogenase. *Science* **2007**, *318*, 1461−1464.
(9) Balasubramanian, R.; Smith, S. M.; Rawat, S.; Yatsunyk, L. A.; Stemmler, T. L.; Rosenzweig, A. C. Oxidation of Methane by a Biological Dicopper Centre. *Nature* **2010**, *465*, 115−119.
(10) Shan, J.; Ye, C.; Chen, S.; Sun, T.; Jiao, Y.; Liu, L.; Zhu, C.; Song, L.; Han, Y.; Jaroniec, M.; Zhu, Y.; Zheng, Y.; Qiao, S.-Z. Short-Range Ordered Iridium Single Atoms Integrated into Cobalt Oxide Spinel Structure for Highly Efficient Electrocatalytic Water Oxidation. *J. Am. Chem. Soc.* **2021**, *143*, 5201−5211.
(11) Rong, X.; Wang, H.-J.; Lu, X.-L.; Si, R.; Lu, T.-B. Controlled Synthesis of a Vacancy-Defect Single-Atom Catalyst for Boosting CO_2 Electroreduction. *Angew. Chem., Int. Ed.* **2020**, *59*, 1961−1965.
(12) Gu, J.; Hsu, C.-S.; Bai, L.; Chen, H. M.; Hu, X. Atomically Dispersed Fe^{3+} Sites Catalyze Efficient CO_2 Electroreduction to CO. *Science* **2019**, *364*, 1091−1094.
(13) Qi, K.; Chhowalla, M.; Voiry, D. Single Atom is not Alone: Metal−Support Interactions in Single-Atom Catalysis. *Mater. Today* **2020**, *40*, 173−192.
(14) Yang, L.; Cheng, D.; Xu, H.; Zeng, X.; Wan, X.; Shui, J.; Xiang, Z.; Cao, D. Unveiling the High-Activity Origin of Single-Atom Iron Catalysts for Oxygen Reduction Reaction. *Proc. Natl. Acad. Sci. U. S. A.* **2018**, *115*, 6626−6631.
(15) Fei, H.; Dong, J.; Chen, D.; Hu, T.; Duan, X.; Shakir, I.; Huang, Y.; Duan, X. Single Atom Electrocatalysts Supported on Graphene or Graphene-Like Carbons. *Chem. Soc. Rev.* **2019**, *48*, 5207−5241.
(16) Li, X.; Liu, L.; Ren, X.; Gao, J.; Huang, Y.; Liu, B. Microenvironment Modulation of Single-Atom Catalysts and Their Roles in Electrochemical Energy Conversion. *Sci. Adv.* **2020**, *6*, No. eabb6833.
(17) Chen, Z.; Vorobyeva, E.; Mitchell, S.; Fako, E.; Ortuño, M. A.; López, N.; Collins, S. M.; Midgley, P. A.; Richard, S.; Vilé, G.; Pérez-Ramírez, J. A Heterogeneous Single-Atom Palladium Catalyst Surpassing Homogeneous Systems for Suzuki Coupling. *Nat. Nanotechnol.* **2018**, *13*, 702−707.
(18) Qin, R.; Liu, K.; Wu, Q.; Zheng, N. Surface Coordination Chemistry of Atomically Dispersed Metal Catalysts. *Chem. Rev.* **2020**, *120*, 11810−11899.
(19) Yi, J.-D.; Xu, R.; Wu, Q.; Zhang, T.; Zang, K.-T.; Luo, J.; Liang, Y.-L.; Huang, Y.-B.; Cao, R. Atomically Dispersed Iron−Nitrogen Active Sites within Porphyrinic Triazine-Based Frameworks for Oxygen Reduction Reaction in Both Alkaline and Acidic Media. *ACS Energy Lett.* **2018**, *3*, 883−889.
(20) Zhang, L.; Jia, Y.; Gao, G.; Yan, X.; Chen, N.; Chen, J.; Soo, M. T.; Wood, B.; Yang, D.; Du, A.; Yao, X. Graphene Defects Trap Atomic Ni Species for Hydrogen and Oxygen Evolution Reactions. *Chem.* **2018**, *4*, 285−297.
(21) Jiao, L.; Jiang, H.-L. Metal-Organic-Framework-Based Single-Atom Catalysts for Energy Applications. *Chem.* **2019**, *5*, 786−804.
(22) Xie, W.; Li, H.; Cui, G.; Li, J.; Song, Y.; Li, S.; Zhang, X.; Lee, J. Y.; Shao, M.; Wei, M. NiSn Atomic Pair on an Integrated Electrode for Synergistic Electrocatalytic CO_2 Reduction. *Angew. Chem., Int. Ed.* **2021**, *60*, 7382−7388.
(23) Jiao, J.; Lin, R.; Liu, S.; Cheong, W.-C.; Zhang, C.; Chen, Z.; Pan, Y.; Tang, J.; Wu, K.; Hung, S.-F.; Chen, H. M.; Zheng, L.; Lu, Q.; Yang, X.; Xu, B.; Xiao, H.; Li, J.; Wang, D.; Peng, Q.; Chen, C.; Li, Y. Copper Atom-Pair Catalyst Anchored on Alloy Nanowires for Selective and Efficient Electrochemical Reduction of CO_2. *Nat. Chem.* **2019**, *11*, 222−228.
(24) Zhou, H.-C.; Long, J. R.; Yaghi, O. M. Introduction to Metal−Organic Frameworks. *Chem. Rev.* **2012**, *112*, 673−674.
(25) Islamoglu, T.; Goswami, S.; Li, Z.; Howarth, A. J.; Farha, O. K.; Hupp, J. T. Postsynthetic Tuning of Metal−Organic Frameworks for Targeted Applications. *Acc. Chem. Res.* **2017**, *50*, 805−813.
(26) Zhao, X.; Wang, Y.; Li, D.-S.; Bu, X.; Feng, P. Metal−Organic Frameworks for Separation. *Adv. Mater.* **2018**, *30*, No. 1705189.
(27) Li, H.; Li, L.; Lin, R.-B.; Zhou, W.; Zhang, Z.; Xiang, S.; Chen, B. Porous Metal-Organic Frameworks for Gas Storage and Separation: Status and Challenges. *EnergyChem.* **2019**, *1*, 100006.
(28) Liu, D.; Wan, J.; Pang, G.; Tang, Z. Hollow Metal−Organic-Framework Micro/Nanostructures and their Derivatives: Emerging Multifunctional Materials. *Adv. Mater.* **2019**, *31*, 1803291.
(29) Ye, Y.; Gong, L.; Xiang, S.; Zhang, Z.; Chen, B. Metal−Organic Frameworks as a Versatile Platform for Proton Conductors. *Adv. Mater.* **2020**, *32*, 1907090.
(30) Jiao, L.; Wang, Y.; Jiang, H.-L.; Xu, Q. Metal−Organic Frameworks as Platforms for Catalytic Applications. *Adv. Mater.* **2018**, *30*, 1703663.
(31) Jiao, L.; Wang, J.; Jiang, H.-L. Microenvironment Modulation in Metal-Organic Framework-Based Catalysis. *Acc. Mater. Res.* **2021**, *2*, 327−339.
(32) Lee, K. J.; Lee, J. H.; Jeoung, S.; Moon, H. R. Transformation of Metal−Organic Frameworks/Coordination Polymers into Functional Nanostructured Materials: Experimental Approaches Based on Mechanistic Insights. *Acc. Chem. Res.* **2017**, *50*, 2684−2692.
(33) Huang, H.; Shen, K.; Chen, F.; Li, Y. Metal−Organic Frameworks as a Good Platform for the Fabrication of Single-Atom Catalysts. *ACS Catal.* **2020**, *10*, 6579−6586.
(34) Guan, A.; Chen, Z.; Quan, Y.; Peng, C.; Wang, Z.; Sham, T.-K.; Yang, C.; Ji, Y.; Qian, L.; Xu, X.; Zheng, G. Boosting CO_2 Electroreduction to CH_4 via Tuning Neighboring Single-Copper Sites. *ACS Energy Lett.* **2020**, *5*, 1044−1053.
(35) Wan, X.; Liu, X.; Li, Y.; Yu, R.; Zheng, L.; Yan, W.; Wang, H.; Xu, M.; Shui, J. Fe−N−C Electrocatalyst with Dense Active Sites and Efficient Mass Transport for High-Performance Proton Exchange Membrane Fuel Cells. *Nat. Catal.* **2019**, *2*, 259−268.

(36) Mohd Adli, N.; Shan, W.; Hwang, S.; Samarakoon, W.; Karakalos, S.; Li, Y.; Cullen, D. A.; Su, D.; Feng, Z.; Wang, G.; Wu, G. Engineering Atomically Dispersed FeN_4 Active Sites for CO_2 Electroreduction. *Angew. Chem., Int. Ed.* **2021**, *60*, 1022−1032.
(37) Jiao, L.; Yang, W.; Wan, G.; Zhang, R.; Zheng, X.; Zhou, H.; Yu, S.-H.; Jiang, H.-L. Single-Atom Electrocatalysts from Multivariate Metal−Organic Frameworks for Highly Selective Reduction of CO_2 at Low Pressures. *Angew. Chem., Int. Ed.* **2020**, *59*, 20589−20595.
(38) Yang, H.; Wu, Y.; Li, G.; Lin, Q.; Hu, Q.; Zhang, Q.; Liu, J.; He, C. Scalable Production of Efficient Single-Atom Copper Decorated Carbon Membranes for CO2 Electroreduction to Methanol. *J. Am. Chem. Soc.* **2019**, *141*, 12717−12723.
(39) Wei, Y.-S.; Zhang, M.; Zou, R.; Xu, Q. Metal−Organic Framework-Based Catalysts with Single Metal Sites. *Chem. Rev.* **2020**, *120*, 12089−12174.
(40) Zhao, C.-X.; Li, B.-Q.; Liu, J.-N.; Zhang, Q. Intrinsic Electrocatalytic Activity Regulation of M−N−C Single-Atom Catalysts for the Oxygen Reduction Reaction. *Angew. Chem., Int. Ed.* **2021**, *60*, 4448−4463.
(41) Asset, T.; Atanassov, P. Iron-Nitrogen-Carbon Catalysts for Proton Exchange Membrane Fuel Cells. *Joule* **2020**, *4*, 33−44.
(42) Yang, S.; Yu, Y.; Dou, M.; Zhang, Z.; Dai, L.; Wang, F. Two-Dimensional Conjugated Aromatic Networks as High-Site-Density and Single-Atom Electrocatalysts for the Oxygen Reduction Reaction. *Angew. Chem., Int. Ed.* **2019**, *58*, 14724−14730.
(43) Huang, X.-C.; Lin, Y.-Y.; Zhang, J.-P.; Chen, X.-M. Ligand-Directed Strategy for Zeolite-Type Metal−Organic Frameworks: Zinc(II) Imidazolates with Unusual Zeolitic Topologies. *Angew. Chem., Int. Ed.* **2006**, *45*, 1557−1559.
(44) Park, K. S.; Ni, Z.; Côté, A. P.; Choi, J. Y.; Huang, R.; Uribe-Romo, F. J.; Chae, H. K.; O'Keeffe, M.; Yaghi, O. M. Exceptional Chemical and Thermal Stability of Zeolitic Imidazolate Frameworks. *Proc. Natl. Acad. Sci. U. S. A.* **2006**, *103*, 10186−10191.
(45) Jiang, H.-L.; Liu, B.; Lan, Y.-Q.; Kuratani, K.; Akita, T.; Shioyama, H.; Zong, F.; Xu, Q. From Metal−Organic Framework to Nanoporous Carbon: Toward a Very High Surface Area and Hydrogen Uptake. *J. Am. Chem. Soc.* **2011**, *133*, 11854−11857.
(46) Zhang, Y.; Jiao, L.; Yang, W.; Xie, C.; Jiang, H.-L. Rational Fabrication of Low-Coordinate Single-Atom Ni Electrocatalysts by MOFs for Highly Selective CO_2 Reduction. *Angew. Chem., Int. Ed.* **2021**, *60*, 7607−7611.
(47) Zhang, B.; Zheng, X.; Voznyy, O.; Comin, R.; Bajdich, M.; Garcia-Melchor, M.; Han, L.; Xu, J.; Liu, M.; Zheng, L.; Garcia de Arquer, F. P.; Dinh, C. T.; Fan, F.; Yuan, M.; Yassitepe, E.; Chen, N.; Regier, T.; Liu, P.; Li, Y.; De Luna, P.; Janmohamed, A.; Xin, H. L.; Yang, H.; Vojvodic, A.; Sargent, E. H. Homogeneously Dispersed Multimetal Oxygen-Evolving Catalysts. *Science* **2016**, *352*, 333−337.
(48) Xie, J.; Wang, Y. Recent Development of CO_2 Electrochemistry from Li−CO_2 Batteries to Zn−CO_2 Batteries. *Acc. Chem. Res.* **2019**, *52*, 1721−1729.
(49) Varela, A. S.; Ju, W.; Bagger, A.; Franco, P.; Rossmeisl, J.; Strasser, P. Electrochemical Reduction of CO_2 on Metal-Nitrogen-Doped Carbon Catalysts. *ACS Catal.* **2019**, *9*, 7270−7284.
(50) Ren, W.; Tan, X.; Yang, W.; Jia, C.; Xu, S.; Wang, K.; Smith, S. C.; Zhao, C. Isolated Diatomic Ni-Fe Metal−Nitrogen Sites for Synergistic Electroreduction of CO_2. *Angew. Chem., Int. Ed.* **2019**, *58*, 6972−6976.
(51) Zheng, T.; Jiang, K.; Wang, H. Recent Advances in Electrochemical CO_2-to-CO Conversion on Heterogeneous Catalysts. *Adv. Mater.* **2018**, *30*, 1802066.
(52) Yang, J.; Qiu, Z.; Zhao, C.; Wei, W.; Chen, W.; Li, Z.; Qu, Y.; Dong, J.; Luo, J.; Li, Z.; Wu, Y. In Situ Thermal Atomization to Convert Supported Nickel Nanoparticles into Surface-Bound Nickel Single-Atom Catalysts. *Angew. Chem., Int. Ed.* **2018**, *57*, 14095−14100.
(53) Schwartz, D. A.; Norberg, N. S.; Nguyen, Q. P.; Parker, J. M.; Gamelin, D. R. Magnetic Quantum Dots: Synthesis, Spectroscopy, and Magnetism of Co^{2+}- and Ni^{2+}-Doped ZnO Nanocrystals. *J. Am. Chem. Soc.* **2003**, *125*, 13205−13218.
(54) Watanabe, M.; Kanno, M.; Ackland, D. W.; Kiely, C. J.; Williams, D. B. Applications of Electron Energy Loss Spectrometry and Energy Filtration in an Aberration-Corrected JEM-2200FS STEM/TEM. *Microsc. Microanal.* **2007**, *13*, 1264−1265.

https://doi.org/10.1021/jacs.1c08050
J. Am. Chem. Soc. 2021, 143, 19417−19424